Optothermal profile of an ablation catheter with integrated microcoil for MR-thermometry during Nd:YAG laser interstitial thermal therapies of the liver—An *in-vitro* experimental and theoretical study

Evdokia M. Kardoulaki,[a)] Richard R. A. Syms, Ian R. Young, and Kaushal Choonee
Department of Electrical and Electronic Engineering, Imperial College London, London SW7 2AZ, United Kingdom

Marc Rea and Wladyslaw M. W. Gedroyc
Department of Radiology, Imperial College Healthcare NHS Trust, Paddington, London W2 1NY, United Kingdom

Purpose: Flexible microcoils integrated with ablation catheters can improve the temperature accuracy during local MR-thermometry in Nd:YAG laser interstitial thermal therapies. Here, the authors are concerned with obtaining a preliminary confirmation of the clinical utility of the modified catheter. They investigate whether the thin-film substrate and copper tracks of the printed coil inductor affect the symmetry of the thermal profile, and hence of the lesion produced.
Methods: Transmission spectroscopy in the near infrared was performed to test for the attenuation at 1064 nm through the 25 μm thick Kapton substrate of the microcoil. The radial transmission profile of an infrared high-power, light emitting diode with >80% normalized power at 1064 nm was measured through a cross section of the modified applicator to assess the impact of the copper inductor on the optical profile. The measurements were performed in air, as well as with the applicator surrounded by two types of scattering media; crystals of NaCl and a layer of liver-mimicking gel phantom. A numerical model based on Huygens–Fresnel principle and finite element simulations, using a commercially available package (COMSOL Multiphysics), were employed to compare with the optical measurements. The impact of the modified optical profile on the thermal symmetry was assessed by examining the high resolution microcoil derived thermal maps from a Nd:YAG laser ablation performed on a liver-mimicking gel phantom.
Results: Less than 30% attenuation through the Kapton film was verified. Shadowing behind the copper tracks was observed in air and the measured radial irradiation correlated well with the diffraction pattern calculated numerically using the Huygens–Fresnel principle. Both optical experiments and simulations, demonstrate that shadowing is mitigated by the scattering properties of a turbid medium. The microcoil derived thermal maps at the end of a Nd:YAG laser ablation performed on a gel phantom in a 3 T scanner confirm that the modified irradiation pattern does not disrupt the thermal symmetry, even though, unlike tissue, the gel is minimally scattering.
Conclusions: The results from this initial assessment indicate that microcoils can be safely integrated with ablation catheters and ensure that the complete necrosis of the liver tumor can still be achieved.

1. INTRODUCTION

Minimally invasive MR-guided thermal therapies are increasingly used to destroy lesions in the liver and considerable efforts are being made to improve their safety and efficacy.[1–15] Given the difficulty of accurately modeling the thermal distribution due to the absorption of photons during laser interstitial thermal therapies (LITTs) with typically inhomogeneous tumor regions surrounded by a complex network of vasculature, MR-guidance of these operations is of utmost importance.

It is clear that earlier thermometry approaches[16] based on thermocouples, Bragg sensors, or fluorooptic sensors in addition to being invasive, cannot provide the required spatiotemporal monitoring. Compared to other noninvasive thermometry methods such as ultrasound thermometry, MR-thermometry can provide high-resolution updates of the spatial thermal profile in close to real-time, while unlike CT-thermometry,[17] it is radiation free.

By accurately monitoring the thermal and structural changes that the tissue undergoes during ablation, it is possible to enable dynamic adaptation of the thermal dose and ensure the complete necrosis of the lesion while sparing the surrounding vital structures. One of the main objectives is to increase the resolution and the accuracy of the temperature

measurement during MR-thermometry. The thermal information can be then used as a feedback for safely adjusting the thermal dose, the position of the ablation catheter, or for introducing additional catheters.

Microcoils colocated with the ablation catheter have the potential to improve the control of MR-guided thermal therapies. It has been convincingly demonstrated that they are inherently less affected by body noise compared to external coils,[18–20] implying that significantly higher signal-to-noise-ratio (SNR) and hence increased temperature accuracy are possible within a small field-of-view (FOV), typically sufficient for the lesion dimensions treated. However, there are only limited studies of their effectiveness for local MR-thermometry.[21–23]

In a recent study,[24] we demonstrated that significant improvements in the overall control of LITTs can result from the integration of flexible microcoils[20] with commercially available laser catheters. The results from an Nd:YAG gel-phantom ablation [where the microcoil proton-resonance frequency (PRF) MR-thermometry performance was compared with that of an array coil] indicated that the SNR and temperature accuracy are improved by ten times within a radius of 20 mm.

Here, we consider how the integration of a microcoil with the ablation catheter can affect the irradiation pattern of a diffusive fibre tip, and we examine the thermal implications by assessing the microcoil derived thermal maps of axial thermometry slices, produced during the Nd:YAG laser ablation in Ref. 24. More specifically, we interpret how the measured and simulated optical profile of the modified catheter correlates with the microcoil derived thermal maps. The effects of the microcoil substrate and printed copper inductor are independently assessed.

2. MATERIALS AND METHODS

2.A. Laser applicator and laser system

A Somatex water-cooled laser applicator (Power-Laser Applicator Set, SOMATEX, Teltow, Germany) and a Nd:YAG laser (MY 30, Marting Medizin-Technik, Tuttlingen, Germany) with a wavelength of 1064 nm and 25 W output power were used for the ablation of a liver-mimicking gel phantom. The laser light was delivered through a 12 m length of fibre with a 400 μm diameter core and a 20 mm diffuser active tip (Surgical Laser Technology). The internal circulation cooling system was maintained by a continuous flow of 0.9% NaCl at a rate of 60 ml/min.

2.B. Integration of the microcoil with the ablation catheter

The microcoil receiver is shown in Fig. 1(a). It is based on a copper-clad Kapton thin film (35 μm thick Cu on 25 μm thick Kapton) and consists of a 60 mm long, 4.5 mm wide, two-turn spiral inductor with a line width of 150 μm. A pair of integrated capacitors C_T and C_M enable tuning and matching, while a subminiature coaxial cable and a non-magnetic pin diode enable active detuning. The details of the modified
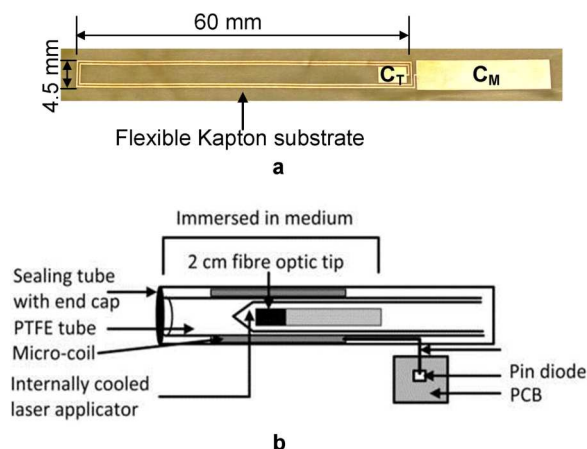

Fig. 1. (a) Flexible microcoil receiver with integrated tuning (C_T) and matching (C_M) capacitors and (b) schematic of a cross section through the modified laser applicator with integrated microcoil receiver.

ablation catheter are shown in Fig. 1(b). A PTFE tube was slid over the applicator and the microcoil, tuned and matched to the loaded condition (at 127.6 MHz), was wrapped around it and held in place with a heat-shrink sleeve, leading to a final diameter of 5 mm. Although this diameter is still sufficient for minimally invasive operations, we are investigating custom made solutions that will further reduce it.

2.C. Gel phantom and experimental setup

The gel phantom with liver-mimicking MR-properties [$T_1 = 800$ ms and $T_2 = 50$ ms (Ref. 24)] was prepared by mixing 31.5 g agar with 58 ml *n*-propanol and 642 ml salt solution, a solution containing 3.37 g/L $NiCl_2.6H_2O$ and 2.4 g/L NaCl. To enable absorption at 1064 nm, the gel was doped with 8% India ink.

The complete setup is shown in Fig. 2(a). The ablation phantom has cylindrical symmetry, with the probe cast horizontally in the middle, as shown in Fig. 2(b) which is a photograph of the phantom mould before casting the ink-doped gel. The cylindrical mould, consisting of 11, 9.5 mm thick Perspex slices has been cast inside clear agar gel which emulates body loading [see Fig. 2(a)].[24] The details of a cross section through the slices that were monitored during the ablation experiment are illustrated in Fig. 2(c).

2.D. Microcoil PRF MR-thermometry

The ablation was carried out in a 3 T GE Signa Excite scanner (GE Healthcare, Milwaukee, WI). A 2D gradient-echo thermometry sequence[10] with repetition time (TR) = 7.976 ms, echo time (TE) = 3.872 ms, flip angle (FA) = 20°, temporal resolution = 6 s, voxel size = 0.47 × 0.47 × 10 mm, FOV = 120 mm, and pixel bandwidth (BW) = 244.141 Hz/pixel was used to monitor the temperature of two axial slices.

The details of the two thermometry slices that were monitored, using PRF MR-thermometry, simultaneously during ablation are illustrated on the schematic of Fig. 2(c). A Luxtron fluorooptic sensor (Luxtron 790, Luxtron, Santa Clara, CA)
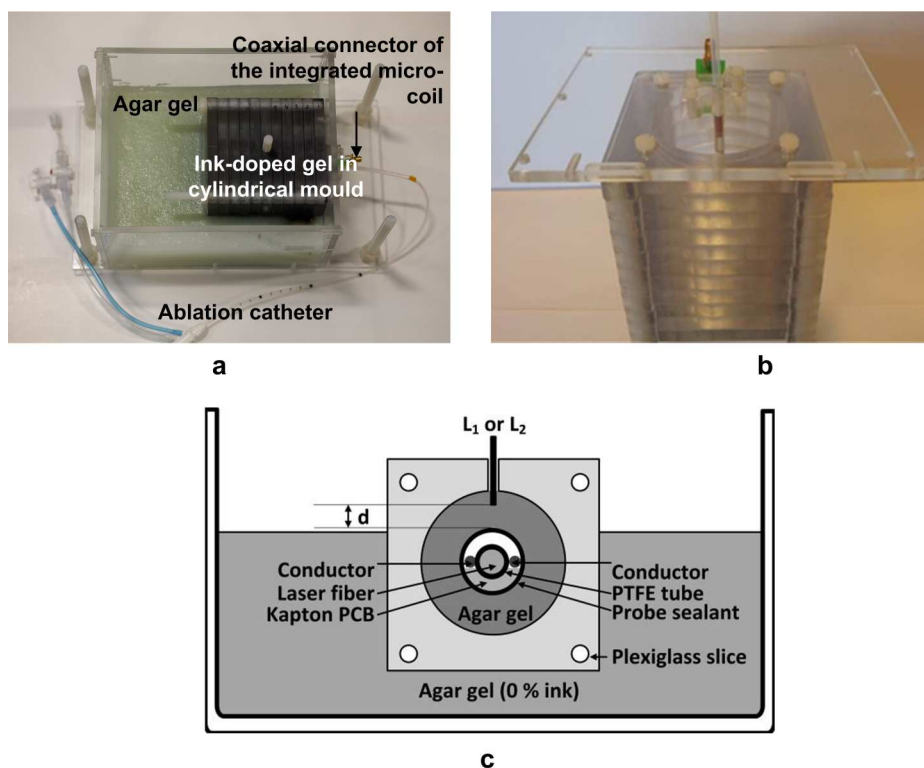
Fig. 2. (a) Complete arrangement for Nd:YAG laser ablation, (b) arrangement of the cylindrical mould before gel casting, and (c) schematic of an axial thermometry slice, showing the details of the microcoil assembly and the position of the Luxtron sensors $L_{1,2}$.

was inserted in each, providing temperature references at two discrete locations [at $d_1 = 5$ mm (L_1) to the probe in slice 1 and at $d_2 = 10$ mm (L_2) in slice 2] during ablation for comparison with the MR-inferred temperatures.

The thermal maps of each slice (containing either L_1 at $d_1 = 5$ mm or L_2 at $d_2 = 10$ mm) were derived offline by postprocessing the acquired phase images in MATLAB™. The pixel-by-pixel values of the phase differences ($\Delta\varphi$) were converted into temperature differences according to Eq. (1).[5] Here, T_{ref} is the temperature recorded with the Luxtron sensors at the beginning of the experiment (baseline), a is the PRF shift coefficient (ppm/°C), $\gamma/360°$ is the gyromagnetic ratio (45. 2 MHz/T), B_0 is the static magnetic field (3 T), and TE is the echo time (3.872 ms). The thermal coefficient a was determined from the linear fit of the phase differences [in the region of interest (ROI) corresponding to L_1], plotted against the temperature differences recorded with L_1. Two non-heated ROIs (10×30 pixels) were used to correct for non-temperature related phase changes

$$T_{(n)} = [\Delta\varphi/(a \cdot \gamma \cdot B_0 \cdot \text{TE} \cdot 360)] + T_{ref}. \qquad (1)$$

2.E. Near infrared transmission spectroscopy of the Kapton film substrate

The transmission spectrum of the 25 μm thick Kapton substrate was measured in the near infrared (NIR) range to determine the absorption at 1064 nm. The setup of Fig. 3 was employed for this measurement. A broadband light source was used and the excitation wavelength was varied

over the range of 600 to 1200 nm in steps of 10 nm, using a computer-controlled monochromator. The transmitted intensity through the film at each wavelength was recorded using a Ge photodetector and a lock-in amplifier as shown in Fig. 3. To determine the absorption, the transmission spectrum through Kapton was normalized to that of air.

2.F. Measured irradiation through the modified catheter

The copper track of the microcoil inductor is 35 μm thick and hence is a perfect conductor at 1064 nm, leading to a region of low optical intensity. The extent of this shadowing effect was assessed by characterizing the radial transmission profile of an infrared high-power, light emitting diode (LED) (M1050F1, Thorlabs) with >80% normalized power at 1064 nm through a cross section of the modified applicator. The LED was coupled to a multimode fiber (MMF), fixed in the
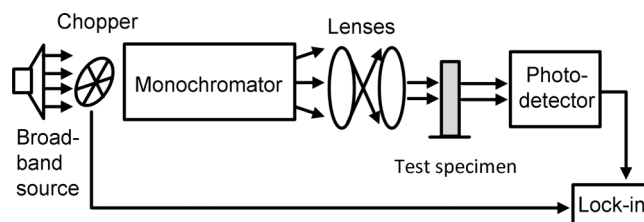

Fig. 3. Experimental set up for near IR transmission spectroscopy of the Kapton film and for the characterization of the absorption coefficient μ_α of the ink-doped ablation gel.
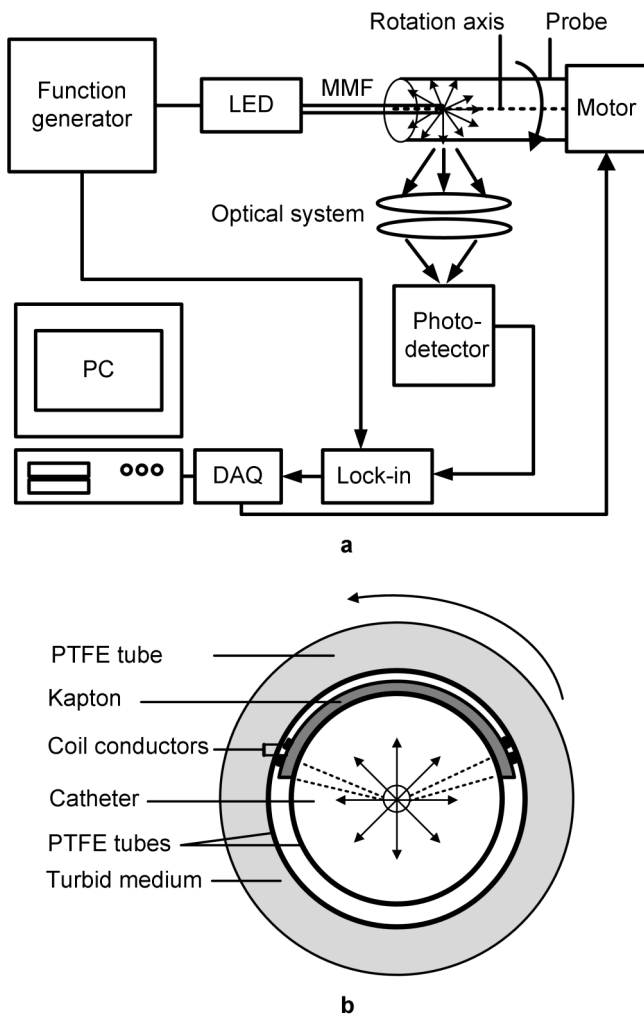
FIG. 4. (a) Arrangement for intensity transmission measurements through the modified ablation catheter, assuming a spatially coherent light source and (b) modified catheter cross section with a surrounding turbid medium.

center of the probe as shown in Fig. 4 and it was driven at a constant current of 50 mA. The diffuse characteristics of the ablation fiber were not emulated in this case, so that the fiber produced a forward propagating collimated and spatially coherent light instead of a diffuse light.

A rotating mechanical shaft, controlled from a PC by means of Labview™ code, allowed for the transmitted light intensity through the probe to be recorded over a full revolution in steps of 2° using an imaging system and a Ge detector perpendicular to the axis of rotation. To reduce noise due to the background light, the detector output was fed into a lock-in amplifier, which was locked to the frequency of a modulating square wave (3 V square wave, with 1 kHz frequency) that was applied to the LED. The measured light intensity was normalized to the intensity without the microcoil. An optical system, consisting of a pair of magnifying lenses, at $d_1 = 6$ mm to the fiber and at $d_2 = 9$ mm to the detector, ensured high spatial resolution.

To determine the extent of shadowing, three measurements of the transmitted light intensity through the modified catheter were performed: (a) in air, (b) with a thin (2 mm) surrounding

layer of scattering medium provided by NaCl crystals, and (c) with a thin (2 mm) surrounding layer of the ink-doped gel in order to compare with the thermal profiles obtained using the microcoil MR-data from the ablation. The absorption coefficient μ_a of the gel was determined as 0.12 mm^{-1} using the setup of Fig. 3 and employing the Beer–Lambert law Eq. (2), where z is the thickness in mm of the cuvette containing the sample, I_o the intensity of light through the empty cuvette, and I the intensity of light through the cuvette filled with the ink-doped gel

$$\mu_a = (1/z)\ln(I/I_o). \tag{2}$$

2.G. Huygens–Fresnel diffraction model

The distribution of light around the opaque copper can be modeled using the Huygens–Fresnel principle. Every point on an optical wavefront can be considered as a source of secondary spherical waves, which interfere with each other to produce a new wavefront at a given distance away. Due to the cylindrical symmetry of the geometry, we considered only the profile through the middle of the inductor, and assumed an infinitely thin inductor. The model was implemented in MATLAB™ for comparison with the measured results of the radial irradiation pattern obtained in air. The diffuse nature of the ablation fiber was incorporated, by considering a spatially incoherent light source.

Every point x_i of the line across the inductor was modeled as a discrete point source of intensity E_o $(x_i,0)$ (V/m) with a random phase φ_i assigned to it. As shown in Fig. 5(a), the intensity E_z $(\xi_k,0)$ at a given point d distance away (in the z-axis) was calculated by summing the contributions from all point sources x_i which were assumed to have intensity equal to 1 (so that attenuation due to the Kapton film was ignored) with the exception of the conductor tracks, where zero intensity was assumed.

The field intensity at a distance d was calculated according to Eq. (3), where $\lambda = 1064$ nm, $k = 2\pi/\lambda$, and $f(\theta) = [1 + \cos\theta]/2$ accounts for backscattering propagation.[25] When diffuse light was considered, the terms exp $(-j\varphi_i)$ in Eq. (3) accounted for a spatially incoherent source and the phase φ_i of each point source x_i was assigned a random value. Otherwise, the phases φ_i, were set to zero

$$E_z(\xi_k,0) = [f(\theta)/(j\lambda d)] \cdot \Sigma_i^N[\exp(-jkx_i) \cdot \exp(-j\varphi_i)]. \tag{3}$$

2.H. Impact of a turbid medium: A multi-parametric study using a full diffraction model

The effect of scattering—a property of a turbid medium such as tissue—on the attenuation of the field intensity behind the conductors was studied through a more realistic planar model of the microcoil developed using a commercially available finite element analysis software package (COMSOL Multiphysics). This allowed the rigorous treatment of diffraction by solving the electromagnetic wave equations for a given
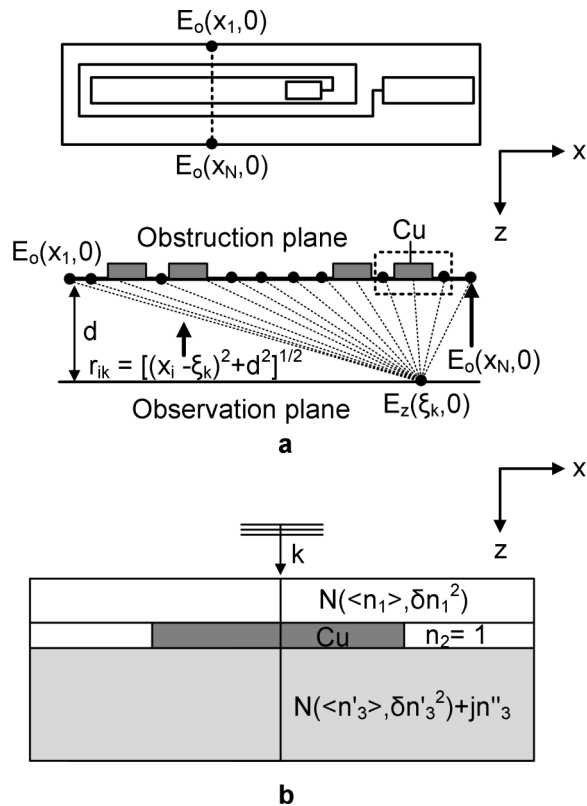
FIG. 5. (a) Schematic of the microcoil, indicating the line across the coil that was considered for the implementation of the numerical diffraction model based on Huygens–Fresnel principle as well as the details of the model and (b) schematic illustrating the details of the full diffraction planar model of the microcoil. Exploiting symmetry in the *x*-axis, only half of one of the four copper tracks [indicated in (a)] has been simulated.

2D geometry of finite thickness, compared to the simpler 1D Huygens–Fresnel model.

The details of the model are illustrated in the schematic of Fig. 5(b). The model shown in Fig. 5(b) is the planar model for one of the inductor tracks as indicated in Fig. 5(a) (dotted line). A plane wave of wavelength of 1064 nm with transverse magnetic (TM) polarization, traveling through a region with refractive index n_1, was assumed to be incident on a 35 μm thick boundary comprising a 75 μm wide metal obstacle, modeling the half width of one of the four copper tracks and a 75 μm wide dielectric of $n_2 = 1$. The dielectric is intended to model a region of Kapton film but it is assumed to be air here in order to study the independent effect of the inductor.

A third region of n_3, below the metal obstacle and dielectric opening, extending up to a depth of 200 μm modeled either a turbid medium or air ($n_3 = 1$). The incident wave travels through the dielectric opening and it is fully absorbed by a perfectly matched layer (PML) at $z = 200$ μm. Perfect magnetic conductor boundaries were used on the left and right boundaries to reflect the symmetry and a mesh size smaller than $\lambda/4$ was used.

Triangular mesh elements were generated by the built-in meshing function and the maximum mesh size was bounded to $\lambda/4$. The upper limit ensures the spatial resolution is

fine enough to accurately capture the wave propagation. Mesh convergence studies were carried out to confirm this. Exploiting symmetry allowed significant reduction in the simulation time.

The following four cases were considered: (a) spatially coherent incident wave and uniform external medium (air), (b) spatially coherent wave and turbid medium, (c) diffuse planar wave and uniform medium (air), and (d) diffuse planar wave and turbid medium. The scattering property of the turbid medium was modeled as random spatial variation $\delta n'$ of the refractive index n' about a mean value $\langle n' \rangle = 1.4$.[26–29] A normal distribution was assumed as codified in Eq. (4) where the variance $\delta n'^2$ reflects the degree of scattering.

Absorption was included in the model by introducing a lossy component $n'' = \mu_\alpha \lambda / 4\pi$ such that $n \sim N(\langle n' \rangle, \delta n'^2) + jn''$. Finally, for a more realistic model, the diffuse nature of the ablation fiber was incorporated by assuming that the region of n_1 through which the incident wave travels before reaching the microcoil interface is also a scattering one. This additional scattering is modeled in the same way as for the tissue region n_3

$$n' \sim N(\langle n' \rangle, \delta n'^2). \tag{4}$$

3. RESULTS

3.A. Symmetry of the thermal profile during ablation

The microcoil derived thermal maps at $t = 10$ min and at $t = 20$ min are shown for each of the two thermometry slices in Fig. 6. In all four cases, the thermal maps are perfectly symmetric as expected from the cylindrical symmetry of the phantom and confirm that the integration of the microcoil did not distort the heating profile.

Figure 7 shows a plot of the MR-inferred temperatures versus the Luxtron data. The readings of the Luxtron sensors are in good agreement with the microcoil MR-inferred temperatures and the temperature standard deviation less than 0.75 °C up to a radius of 20 mm[24] while the phase noise does not exceed 0.5° in a 15×15 mm ROI centered at the catheter. Worth noting that no artifacts due to the Luxtron sensors were observed, neither did the laser fiber affect the Luxtron readings. In our case, the closest distance of the Luxtron sensor to the laser fiber is 5 mm which is larger than the distance at which others have observed effects.[16]

3.B. Transmission spectroscopy of the Kapton film substrate and thermal implications

The transmission spectrum of Kapton between 600 and 1200 nm wavelength is shown in Fig. 8. At 1064 nm, over 70% is transmitted, confirming the expected low absorption of Kapton at the wavelength of interest.[30,31] With a laser power of 25 W, approximately half of the power would pass through the Kapton film, and almost 30% of that fraction would be absorbed, implying that approximately 4 W would be dissipated on the 25 μm thick Kapton film.

Slice 1: Temperature map at t=10 min

a

Slice 1: Temperature map at t=20 min

b

Slice 2: Temperature map at t=10 min

c

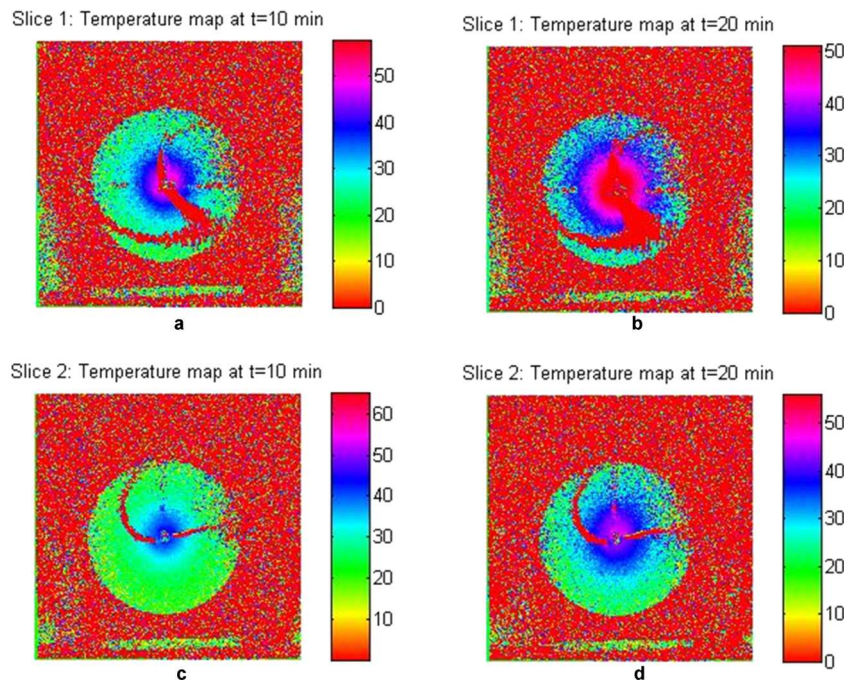Slice 2: Temperature map at t=20 min

d

FIG. 6. Microcoil derived thermal maps employing PRF MR-thermometry: (a) map of the thermometry slice showing Luxtron sensor L_1 after 10 min from the start of the ablation and (b) at the point the laser was turned off; (c) and (d) show respective thermal maps for the thermometry slice corresponding to sensor L_2.

To appreciate the possible thermal implications of absorption in the Kapton film, we also examined the thermal maps shortly after the laser was turned on. Figure 9 shows the microcoil derived thermal maps of the thermometry slice containing L_2 in a 23×23 mm ROI at $t = 2$ min and at $t = 3$ min as well as the corresponding magnitude baseline image that indicates the location of the microcoil on the probe.

At $t = 2$ min, there is a clear elevation of temperature in the region of the Kapton film compared to the upper part of the probe. This temperature difference leads to an initial asymmetric thermal profile in the immediate vicinity of the catheter. The temperature difference is, however, only equal to 3 °C.

The temperature map one minute later ($t = 3$ min) indicates that the asymmetry is no longer present and one possible explanation is the effect of the water cooling system which

does not allow a large thermal gradient to develop between the two parts of the probe.

3.C. Shadowing due to the copper inductor and thermal implications

Figure 10(a) shows the transmitted light over a full revolution of the modified catheter cross section in air, plotted together with the theoretical profile based on Huygens–Frensel principle for $d = 8$ mm [see Fig. 5(a)]. Figure 10(b) presents the profiles with the surrounding layers of ink-doped gel and NaCl crystals. All measured profiles have been normalized to the transmitted light through the original catheter.

Since $d >>$ the 35 μm thick copper conductor, our assumption to neglect the finite thickness and assume an infinitely thin inductor is valid. This is also verified by the excellent correlation of the model results in air with
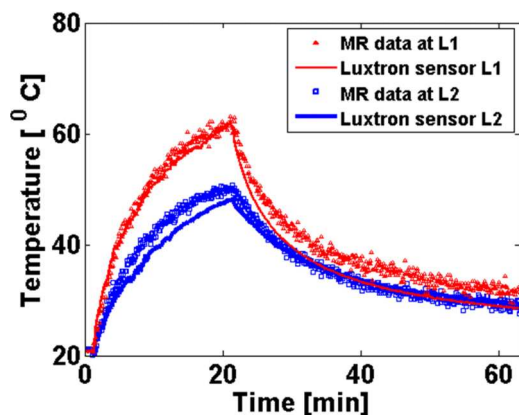

FIG. 7. Comparison of MR-inferred transient temperatures with the fluorooptic readings $L_{1,2}$.
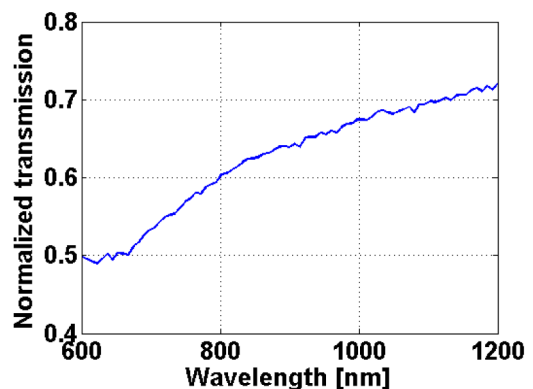

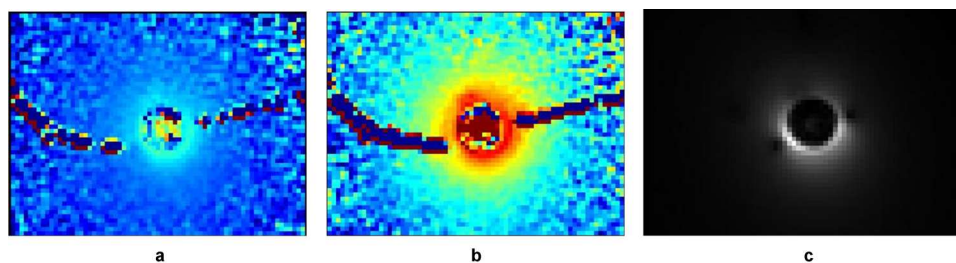FIG. 8. Near IR transmission spectrum of a 25 μm thick Kapton film.

FIG. 9. Thermal maps in a 23×23 mm ROI of the thermometry slice containing L_2 centered at the probe: (a) at $t = 2$ min, (b) at $t = 3$ min, and (c) corresponding magnitude baseline image.

the experimental results (with the exception of the Kapton absorption which is not taken into account). The optical notches around 30° and 150° correspond to the copper tracks which as expected block light. Our optical system provided enough resolution to separate the effect of all four tracks of the two-turn spiral coil. Light is blocked over an angle of 30° at the two regions of the copper tracks and this corresponds to an arc length of 1 mm, assuming the coil is wrapped on a catheter with 4 mm diameter.

The measurement with the thin surrounding layer of ink-doped gel resulted in the same irradiation profile as that obtained in air. Referring to the thermal maps of Fig. 6 (at $t = 10$ min and $t = 20$ min) as well as to the thermal maps at the start of the ablation, shown in Figs. 9(a) and 9(b), there is no thermal effect due to the optical notching. This implies that heat conduction must rapidly prevent the development of a thermal gradient.

In the case of the purely scattering surrounding medium, the irradiation profile is very different. Shadowing is effectively countered due to scattering, and this suggests that the ink-doped gel must be minimally scattering. The mechanism by which scattering counters shadowing is further investigated in Sec. 3.D.

3.D. Simulation results: A multi-parametric study using a full diffraction model

The calculated electric field below the metal–dielectric boundary is shown in Fig. 11 for three different conditions

of scattering for the region of n_3, namely $\delta n_3' = 0$, 0.05, and 0.1. The figures illustrate the results for the left hand side of the model in Fig. 5(b). The right hand side has been taken into account by imposing appropriate boundary conditions as explained in Sec. 2. Figures 11(b)–11(d) correspond to a spatially coherent plane wave and Figs. 11(e)–11(g) to a diffuse wave, modeled by a standard deviation (std) $\delta n_1' = 0.1$.

Our model verifies that scattering redistributes photons from the plane wave that traveled in medium 3 through medium 2, resulting in a nonzero field in the region immediately below the metal obstacle. The E-field increases more than twofold in the case of increased scattering while below medium 2, scattering does not affect the value of the E-field. The use of diffuse illumination does not have a significant effect when scattering is present. In air, however, it leads to a slightly increased field away from the metal boundary compared to the coherent source case. It should be noted that this effect could not be captured through the Huygens–Fresnel model, where there appeared to be no dependence in shadowing on the illumination. A plausible explanation could be the different implementation of a diffuse source in the two cases.

To allow more direct comparison with the optical measurements and thermal maps, we also introduced absorption in region 3. We tested two scenarios: (a) $\mu_\alpha = 0.12$ mm^{-1} by setting and $n_3'' = 10^{-6}$ (a realistic case) and (b) $\mu_\alpha \gg 0.12$mm^{-1} by setting $n_3'' = 0.0013$. The mechanism of scattering in countering shadowing is not affected in the low-loss case ($\mu_\alpha = 0.12$ mm^{-1}). With significant absorption on
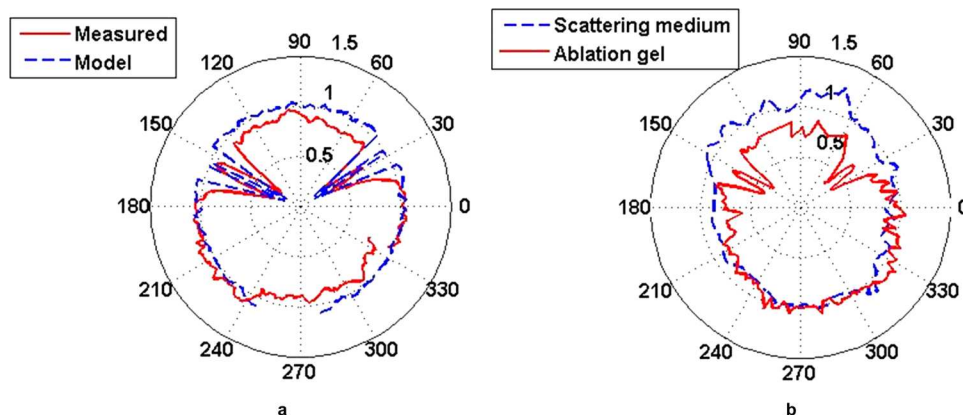

FIG. 10. Normalized intensity transmission profiles through the modified catheter (a) in air versus the Huygens–Fresnel model with a spatially incoherent source and (b) with surrounding scattering medium/ablation gel.
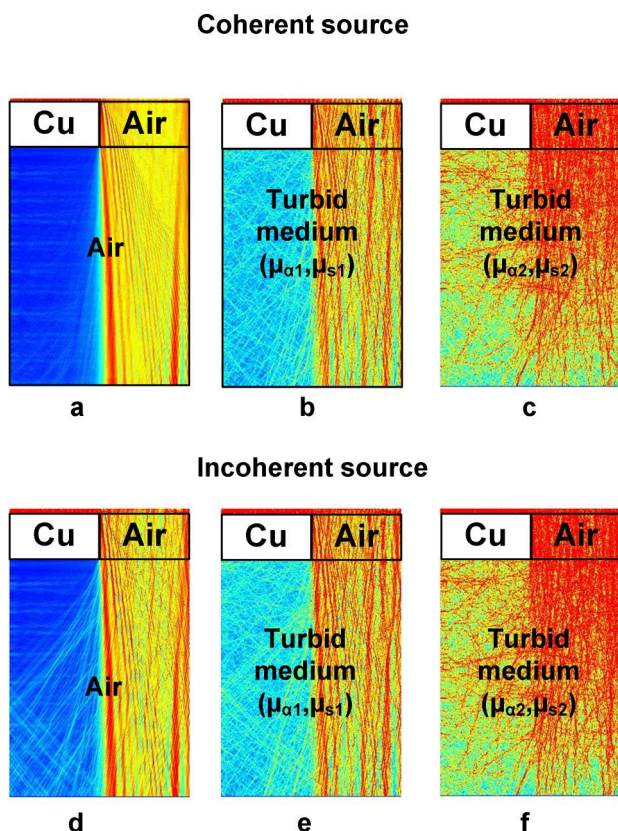
Coherent source

Incoherent source

Fig. 11. Computed 2D electric field distribution for the left hand side of the geometry shown in Fig. 5(a) for a coherent plane wave with (a) $\delta n'_3 = 0$, (b) $\delta n'_3 = 0.05$, (c) $\delta n'_3 = 0.1$ and for a diffuse wave ($\delta n'_1 = 0.1$) with (d) $\delta n'_3 = 0$, (e) $\delta n'_3 = 0.05$, (f) $\delta n'_3 = 0.1$.

the other hand, scattering fails to counter the shadowing below the metal. Absorption seems to be the dominant effect in determining the value of the *E*-field in that case.

These results correlate extremely well with the optical measurements. Although the thermal maps from the gel phantom ablation did not indicate any thermal effect due to the optical notching we observed in the transmission measurements, the simulations further ensure that the shadowing will be minimized due to the scattering properties of tissue.

4. DISCUSSION

We have studied the independent and combined impact of the Kapton substrate and copper tracks on the irradiation pattern of the modified catheter. We have verified through a liver-mimicking phantom Nd:YAG laser ablation, optical measurements, and electromagnetic simulations that the modification of the catheter does not affect the thermal profile. Absorption due to the thin film substrate is low and leads to insignificant heating and the shadowing caused by the conductor tracks is countered by tissue scattering, which acts to redistribute the light.

Despite the simplistic 1D Huygens–Fresnel model, which assumed an infinitely thin coil structure, the shadowing effect behind the copper tracks was captured fairly accurately and

the results of the model correlated really well with the experimental results [see Fig. 10(a)] which accounted for the physical structure of the microcoil. The microcoil thickness was considered in the more complete 2D electromagnetic model of diffraction we used to simulate the effects of scattering and absorption of a turbid medium on a plane electromagnetic wave propagating through the microcoil into the turbid medium.

We modeled tissue scattering as a spatial variation of the refractive index as previously proposed in Refs. 26–29, while liver tissue absorption was modeled as a lossy component of the refractive index, based on the measured value of the absorption coefficient of the liver-mimicking gel phantom. Although these parameters are semi-empirical, they have provided reasonable qualitative answers which were further validated by experimental results.

The excellent sensitivity of the microcoil (see Fig. 7) allowed for an accurate assessment of the thermal profile of the modified catheter without the need for a thermal model. The symmetry of the thermal maps, where the effects of substrate absorption and track obstruction are combined, indicates that any small remaining inhomogeneity of irradiation is most likely corrected by the heat conduction under the operation of the water cooling system of the applicator.

Although more thorough testing will be required using porcine liver, our MR-data based on the gel ablation indicate that Kapton absorption will not compromise tissue necrosis due to exposure to different temperatures neither will it pose a safety risk due to overheating. In the unlikely case of a failure of the water-cooling system during an ablation, undesirable effects such as tissue charring, significantly reduced lesion size, and potentially serious patient safety risk are expected weather a microcoil has been integrated or not with the catheter.[32,33]

5. CONCLUSION

Microcoils, which can easily be integrated with ablation catheters, can improve the control of laser interstitial thermal therapies, and lead to excellent signal-to-noise ratio and temperature accuracy during local MR-thermometry within a radius matching typical lesion dimensions. Here, we have considered the additional effects of microcoil integration on the optothermal performance of the modified catheter. The results of this study provide a preliminary confirmation of the clinical utility of the modified catheter in liver LITTs.

a)Author to whom correspondence should be addressed. Electronic mail: ek03@ic.ac.uk

[1] C. Brace, "Thermal tumor ablation in clinical use," Pulse, IEEE **2**(5), 28–38 (2011).

[2] M. Diakite *et al.*, "Irreversible change in the T1 temperature dependence with thermal dose using the proton resonance frequency-T1 technique," Magn. Reson. Med. **69**, 1122–1130 (2013).

[3] B. Bazrafshan *et al.*, "Temperature imaging of laser-induced thermotherapy (LITT) by MRI: Evaluation of different sequences in phantom," Laser. Med. Sci. **29**(1), 173–183 (2014).

[4] B. Bazrafshan *et al.*, "A liver-mimicking MRI phantom for thermal ablation experiments," Med. Phys. **38**, 2674–2684 (2011).

[5] V. Rieke and K. Butts Pauly, "MR thermometry," J. Magn. Reson. Imaging **27**, 376–390 (2008).

[6] A. Kickhefel *et al.*, "A pilot study for clinical feasibility of the near-harmonic 2D referenceless PRFS thermometry in liver under free breathing using MR-guided LITT ablation data," Int. J. Hyperthermia **28**, 250–266 (2012).

[7] D. Schlesinger *et al.*, "MR-guided focused ultrasound surgery, present and future," Med. Phys. **40**(8), 080901 (32pp.) (2013).

[8] C. Weidensteiner *et al.*, "Stability of real-time MR temperature mapping in healthy and diseased human liver," J. Magn. Reson. Imaging **19**, 438–446 (2004).

[9] A. Kickhefel *et al.*, "Correction of susceptibility-induced GRE phase shift for accurate PRFS thermometry proximal to cryoablation iceball," Magn. Reson. Mater. Phys. **25**, 23–31 (2012).

[10] A. H. Chung *et al.*, "Optimization of spoiled gradient-echo phase imaging for in vivo localization of a focused ultrasound beam," Magn. Reson. Med. **36**, 745–752 (1996).

[11] J. D. Poorter *et al.*, "Noninvasive MRI thermometry with the proton resonance frequency (PRF) method: In vivo results in human muscle," Magn. Reson. Med. **33**, 74–81 (1995).

[12] J. C. Hindman, "Proton resonance shift of water in the gas and liquid states," J. Chem. Phys. **44**, 4582–4592 (1966).

[13] F. Maier *et al.*, "Velocity navigator for motion compensated thermometry," Magn. Reson. Mater. Phys. **25**, 15–22 (2012).

[14] S. M. Sprinkhuizen *et al.*, "Temperature dependence of the magnetic volume susceptibility of human breast fat tissue: An NMR study," Magn. Reson. Mater. Phys. **25**, 33–39 (2012).

[15] M. N. Streicher *et al.*, "Effects of air susceptibility on proton resonance frequency MR thermometry," Magn. Reson. Mater. Phys., Biol. Med. **25**, 41–47 (2012).

[16] P. Saccomandi, E. Schena, and S. Silvestri, "Techniques for temperature monitoring during laser-induced thermotherapy: An overview," Int. J. Hyperthermia **29**(7), 609–619 (2013).

[17] F. Fani *et al.*, "CT-based thermometry: An overview," Int. J. Hyperthermia **30**(4), 219–227 (2014).

[18] Y. Eryaman, Y. Öner, and E. Atalar, "Design of internal MRI coils using ultimate intrinsic SNR," Magn. Reson. Mater. Phys. **22**, 221–228 (2009).

[19] D. I. Hoult and P. C. Lauterbur, "The sensitivity of the zeugmatographic experiment involving human samples," J. Magn. Reson. **1969**(34), 425–433 (1979).

[20] R. R. A. Syms *et al.*, "Thin-film detector system for internal magnetic resonance imaging," Sens. Actuators, A **163**, 15–24 (2010).

[21] M. Rata *et al.*, "Endoluminal ultrasound applicator with an integrated RF coil for high-resolution magnetic resonance imaging-guided high-intensity contact ultrasound thermotherapy," Phys. Med. Biol. **53**, 6549–6567 (2008).

[22] N. A. Volland *et al.*, "Initial feasibility testing of limited field of view magnetic resonance thermometry using a local cardiac radiofrequency coil," Magn. Reson. Med. **70**, 994–1004 (2013).

[23] I. P. Wharton *et al.*, "Design and development of a prototype endocavitary probe for high-intensity focused ultrasound delivery with integrated magnetic resonance imaging," J. Magn. Reson. Imaging **25**, 548–556 (2007).

[24] E. M. Kardoulaki *et al.*, "MR-thermometry with a flexible micro-coil during a Nd:YAG laser ablation on a gel phantom," in *ISMRM-ESMRMB Joint Annual Meeting* (ISMRM, Milan, Italy, 2014), pp. 10–16.

[25] H. C. Van de Hulst, *Light Scattering by Small Particles* (Wiley, New York, 1957).

[26] J. Schmitt and G. Kumar, "Turbulent nature of refractive-index variations in biological tissue," Opt. Lett. **21**, 1310–1312 (1996).

[27] Z. Wang, "Tissue refractive index as marker of disease," J. Biomed. Opt. **16**(11), 116017 (2011).

[28] F. Asllanaj, "Radiative transfer equation for predicting light propagation in biological media: Comparison of a modified finite volume method, the Monte Carlo technique, and an exact analytical solution," J. Biomed. Opt. **19**(1), 15002–15010 (2014).

[29] A. Doronin, C. Macdonald, and I. Meglinski, "Propagation of coherent polarized light in turbid highly scattering medium," J. Biomed. Opt. **19**(2), 025005 (2014).

[30] R. French *et al.*, "Optical properties of polymeric materials for concentrator photovoltaic systems," Sol. Energy Mater. Sol. Cells **95**, 2077–2086 (2011).

[31] P. Dyer, M. Pervolaraki, and T. Lippert, "Experimental studies and thermal modelling of 1064-and 532-nm Nd: YVO4 micro-laser ablation of polyimide," Appl. Phys. A **80**, 529–536 (2005).

[32] K. V. Larin, I. V. Larina, and R. O. Esenaliev, "Monitoring of tissue coagulation during thermotherapy using optoacoustic technique," J. Phys. D: Appl. Phys. **38**, 2645–2653 (2005).

[33] S. G. Nour *et al.*, "MRI-guided and monitored laser ablation for Renal Malignancy: A step toward moving interventional MRI technology to mainstream usage?," in *ISMRM-ESMRMB Joint Annual Meeting* (ISMRM, Milan, Italy, 2014), pp. 10–16.